Multiphysics modeling and experimental validation of heat and mass transfer for the vacuum induction melting process

P. Garcia-Michelena[1*], E. Ruiz-Reina[2], N. Herrero-Dorca[1], X. Chamorro[1]

[1] Mechanical and Manufacturing Department, Mondragon University, Mondragon, 20500, Spain.

[2] Institute Carlos I for Theoretical and Computational Physics (iC1), Department of Applied Physics II, Universidad de Málaga, Málaga, 29071, Spain.

*corresponding author: pgarciam@mondragon.edu Tel. +34 674062456

Highlights

- Development of a multiphysics model for Inconel 718 vacuum induction melting.
- The moving mesh approach effectively reproduces the free surface profile.
- Correlation of the model melt temperatures with the transient measurements.
- Crucible is critical for melt temperature uniformity and heat transfer dynamics.

Abstract

Vacuum induction melting is crucial in casting nickel-based superalloy components, ensuring excellent properties for aero-engine applications. Precise melting temperatures are vital for achieving optimal metallurgical quality before casting. Hence, a multiphysics numerical model is developed to simulate the induction melting process for the Inconel 718 superalloy. The proposed holistic model integrates magnetic fields, induced currents, and heat and momentum transfer phenomena in a single coupled model. A moving mesh approach reproduces the magneto-hydrodynamic behavior of the free surface, simulating the oscillations of the melt. The stabilized deformed surface profile is correlated with experimental measurements, reporting a proper correlation. Then, the flow field and recirculation effect are modeled with a Low Reynolds Number turbulence approach and coupled with the melt convective heat transfer, developing a complete magneto-thermo-hydrodynamic model. In a laboratory-scale vacuum induction melting furnace, transient melting operation variables are characterized and introduced to the numerical model to compute the temperature evolution. An accurate reproduction of the transient melt temperature variations is reported with a relative error of less than 5%. The influence of the crucible thermal insulating capacity is assessed, emissivity dependence evaluated, and melt homogenization is reported at different process stages. This comprehensive numerical and experimental approach offers valuable insights for enhancing vacuum induction melting for Ni-based superalloys.

Keywords: vacuum induction melting; multiphysics modeling, experimental validation, turbulent heat transfer, dynamic modeling, moving mesh

1. Introduction

Nickel-based superalloys are widely used in high-value applications, such as aero-engine turbine components, due to their excellent mechanical properties and high-temperature corrosion resistance [1]. Among them, Inconel 718 excels due to its excellent mechanical properties and cost ratio [2]. Achieving components with the required composition and microstructure, free of metallurgical defects, necessitates advanced manufacturing processes. Vacuum Induction Melting (VIM) [3] is a suitable process for this purpose; however, it presents inherent challenges, including the control and optimization of the process due to the vacuum conditions, magnetic fields, and high melting temperatures.

Numerical models that accurately reproduce the induction melting process are effective tools, offering flexibility, accuracy, and cost-effectiveness. The induction melting process involves magnetic fields, currents, liquid metal flow transport, heating, and heat loss. The time-harmonic magnetic field generated by the alternating current induces a voltage in the melt, leading to eddy currents and subsequent heat generation. Additionally, the Lorentz force results in recirculating metal flow movement that also deforms the top surface of the liquid metal charge. Heat loss occurs through conduction from the charge to the water-cooled coils and radiation mainly from the top surface. Therefore, numerical models must compute the magnetic and thermo-fluid fields and their interactions.

Previous numerical investigations have primarily focused on momentum transport phenomena, particularly the turbulence behavior of the flow. Reynolds-Averaged Navier Stokes (RANS) models have been commonly used, although there is no consensus among authors, with adaptations made to suit specific cases [4]. Various modifications to the standard k-ε model have been proposed to improve agreement with experimental results [5]. Alternative models, such as the k-ω model, have shown promise in reproducing the flow structure and velocity profiles [6]. Large Eddy Simulation (LES) models have also been employed as an alternative to two-equation turbulence models, revealing periodic instabilities in line with experimental findings [7]. Umbrashko et al. studied a 3D LES transient of the turbulent flow and revealed large-scale periodic instabilities with the same frequency as the inductor current, which was in line with experimental results [4].

Further research involved incorporating additional features related to the melting process. The evaporation of alloying elements has garnered significant interest, prompting the advancement of numerical models capable of determining the evaporation rate [8]. Additionally, the stationary distribution of inclusions or alloying elements using particle tracing methods has been considered and experimentally correlated [9]. Related to inclusions, the salty or oxide layer added on the top surface of the melt to improve refining has been considered, including the mass transport between the two phases [10].

In addition to flow phenomena, complex numerical models have been developed to simulate the liquid metal-free surface dynamics in induction melting furnaces. These models utilize fixed mesh approaches, such as the Volume of Fluid (VOF) [11] phase field (PF) [12] or level set method (LSM) [13], to compute the multi-phase air-metal domains and the interphase. However, it necessitated the use of two independent software and meshes to compute the magnetic flux density field and flow field separately, coupled with an internally established program. Similarly, Bansal et al. [14] adopted a comparable strategy employing the fixed mesh method and incorporating the contribution of superficial tension due to the effect of the oxide layer. However, fixed

mesh techniques are computationally intensive and susceptible to interphase diffusion, leading to uncertainties [15].

In regards to electromagnetic induction heating, it has undergone extensive study [16], standing out due to the nonlinear characteristics of the magnetic and thermal aspects, increasing notably the difficulty of its modeling [17]. The skin effect determines heating and flow acceleration in the melt, depending on the alternating current frequency and the material properties of the electrically conducting medium [18]. Magnetic fields are typically defined and solved in the harmonic frame, while thermal problems operate on seconds or minutes timescales [19]. Coupled models iterate between determining the magnetic field based on temperature-dependent material properties and advancing the temperature solution based on the resulting Joule loss distribution [20]. The electromagnetic problem is discretized in the inductors, while the thermal problem focuses on the workpiece [21].

Prior research has examined the influence of various factors on the induction heating process. For instance, the heating pattern and uniformity within the workpiece have been analyzed for different height-diameter ratios and coil shapes [22] [23]. Concerning coil configurations and magnetic induction, different coil structures were studied by Fu et al. [24], who remarked that the longitudinal magnetic flux coil improved heating efficiency and temperature distribution. Temperature inhomogeneity is one of the disadvantages of induction heating; Xiao et al. [25] implemented a frequency conversion method raising an electric-magnetic-thermal coupling model for heating welded, reducing the surface-to-inner side temperature difference.

Another essential feature, the importance of alternating current frequency, has been remarked upon by various previous studies. A novel dual-frequency asynchronous bevel induction heating method has been proposed to improve the temperature uniformity for complex surface workpieces [26]. For high-frequency operation conditions, the melting of titanium wires was numerically developed and partially validated by measuring the instantaneous liquid metal drops temperature [27].

Regarding numerical and experimental correlation, Fisk validated simulations and measurements for Inconel 718 superalloy induction heating, employing a PID (Proportional-Integral-Derivative) controller. This implementation demonstrated a good agreement in temperature estimation [28]. In addition to thermocouple temperature measurements, Kranjc et al. utilized thermographic temperature images, obtaining favorable agreement with numerical results [29].

Notably, these studies have primarily focused on solid-state induction heating, and limited research has been done to couple the heat transfer and the flow field for liquid metals, principally due to the technical difficulties involved due to high melting temperatures and magnetic fields. Previous work by Bulinski et al. [30] successfully modeled a vacuum induction melting furnace for aluminum melt for a fixed applied power. Similarly, ISM (induction skull melting) technology models have been conducted [31] [32], which are capable of relating the temperature response of the model with immersion thermocouple temperature measurements under steady-state conditions [33]. These studies did not consider the higher melting temperatures of Ni-based superalloys and the required transient melt power-temperature adaptations for current industrial casting procedures [34].

Therefore, this study aims to develop a holistic and experimentally validated multiphysics-coupled numerical model utilizing the Finite Element Method (FEM) to simulate the induction melting process for Inconel 718. The numerical model includes all

the physical phenomena and their mutual interaction. The magnetic field is reproduced, introducing the coil features and input power as the source term to compute induced currents and Lorentz forces acting as the inertial term for the flow transport.

The research uses an efficient modeling approach to accurately assess a moving mesh method to reproduce free surface hydrodynamics. The turbulent behavior of the melt has been modeled with a low Reynolds number turbulence approach reproducing the melt recirculation or stirring and the consequent turbulent heat transfer based on the turbulent Prandtl number to account for the heat flux. The model integrates transient and variable operating conditions to replicate actual industrial melting conditions of Ni-based superalloys faithfully.

Two laboratory-scale induction-melting furnaces, operating in distinct environments—one in an open-air setting and the other under a vacuum atmosphere—serve as references for both modeling and melting trials. To enhance modeling precision, specialized equipment has been developed to measure melting variables. With the ad-hoc designed and completed trials, valuable experimental data is collected from these arrangements, which will be utilized to validate the numerical model, assess its accuracy, and evaluate improvement potential.

2. Numerical modeling

2.1 Geometry and assumptions

A semi-industrial VIM facility manufactured by Seco/Warwick S.A. was considered a reference for the numerical modeling and posterior experimental measurements. The VIM furnace comprises an airtight steel chamber connected to a vacuum system. The melt-box (Fig. 1), with a 2 kg melting capacity of nickel-based superalloys, consists of a sinusoidal coil and a crucible covered with housing. The copper coaxial coil is connected to a power generator with a nominal capacity of 100 kW at 10 kHz. The coaxial coil is water-cooled and refrigerated by a chiller. The refractory protection consists of two layers: an active layer to contain the metal, a crucible made of Al_2O_3, and a reinforcing layer composed of Al_2O_3-CaO.

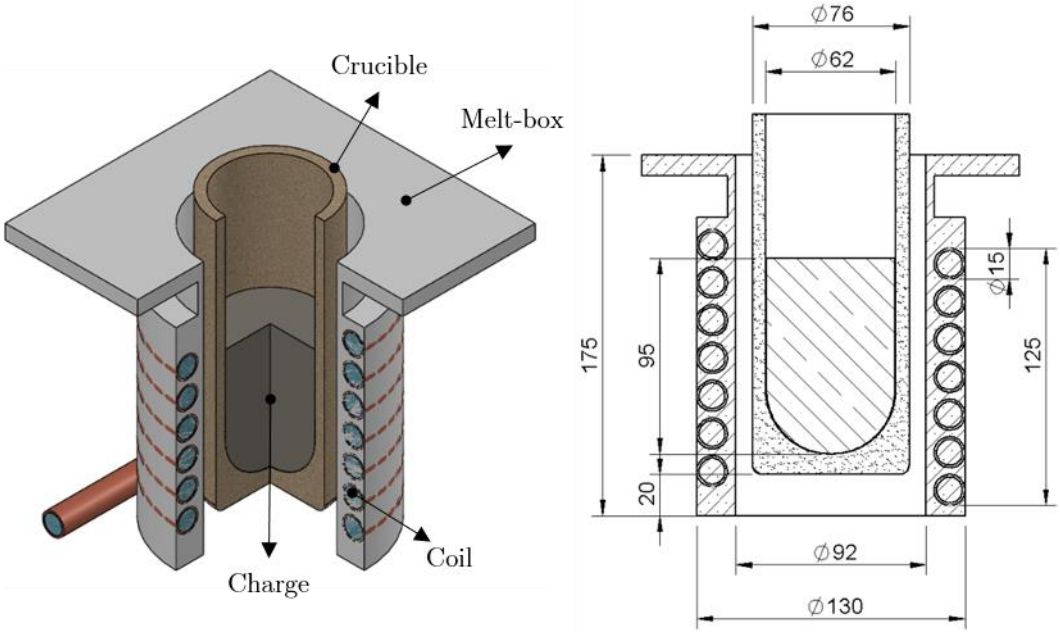

Fig. 1. 3D melt-box and section view of the geometry with principal dimensions.

The model's geometry was reduced to a two-dimensional axisymmetric plane, exploiting the axial symmetry and periodicity of the melt-box. The alternating current passing through the coil was periodic, and the coil's electrical variables were constant for each power provided by the generator. The metal was assumed to be initially completely liquid, not accounting for the solid-liquid phase change effects nor the posterior mold casting and related solidification. Also, it was presumed that due to the vacuum atmosphere, there was no presence of oxide particles on the free surface of the melt.

The partial differential equations (PDEs) that describe the physical phenomena were discretized with the FEM based on COMSOL Multiphysics® v.6.0. The domains and boundaries considered in the model are summarized in Fig. 2.

Domain	Description
A	Vacuum Atmosphere
B	Chamber Structure
C	Liquid Metal
D	Crucible
E	Vacuum/Air
F	Melt-box
G	Coil
H	Refrigeration water
Boundary	**Description**
1	Symmetry axis
2	Chamber inner contour
3	Metal-free surface
4	Crucible internal wall
5	Crucible open boundary
6	Melt-box outer contour
7	Coil refrigeration contour

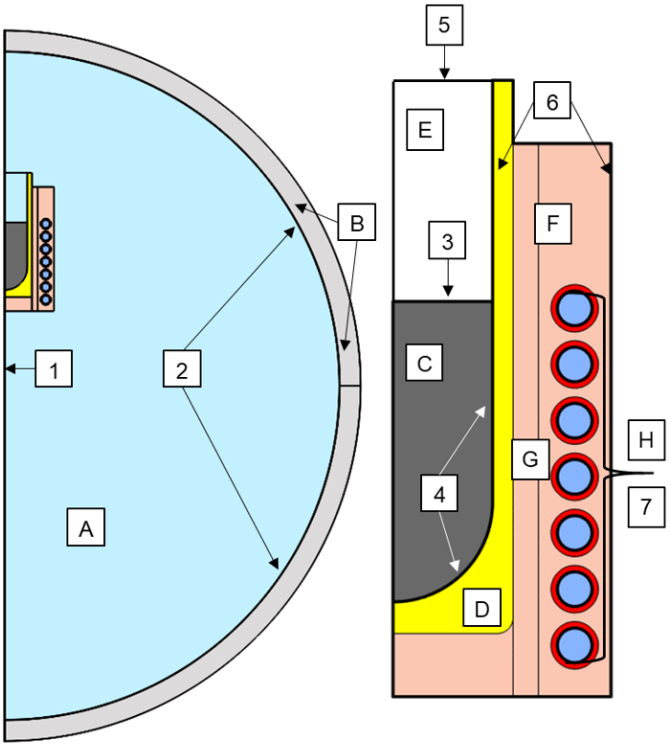

Fig. 2. Resume of model domains and boundaries for the model geometry.

The magnetic field was computed for all domains, and the fluid velocity field was calculated in the melt, with heat transfer simulated in the complete melt-box, crucible, coil, and metal. Due to the difference in timescales between magnetic induction, heat transfer, and flow transport, the first was solved for the frequency domain and the latter for the temporal frame. The details of the implemented equations are described in the following section.

The numerical modeling was divided into two sub-models for an efficient simulation. The first sub-model considers only the magnetic-hydrodynamic coupling and the moving mesh interface to simulate the free surface deformation of the melt until reaching a fixed free surface shape at a constant applied power. The averaged flow field and turbulence field were computed with the standard $k-\varepsilon$ model. The free surface instabilities of the melt were neglected.

Once a stationary situation was reached, the second sub-model, magneto-thermo-hydrodynamic, was solved where the thermal field was coupled while maintaining the top free surface static. The melt heating and heat losses were computed in this second model. The flow field and heat transfer can be coupled based on the turbulent Prandtl

number model, and the turbulence was resolved with a low Reynolds number approach for a more accurate flow field resolution.

The considered heat losses were conduction and radiation. The first heat flux direction was from the melt passing through the crucible and melt box to dissipating in the water-refrigerated coil. Second, the top free surface radiation was described using the Stefan-Boltzmann law, which establishes the emissivity and the surface temperature of the melt. The radiation heating contribution of the surroundings to the melt was neglected. It was assumed that the chamber had a perfect vacuum condition; thus, the air convective effects were disregarded.

2.2 Magneto-hydrodynamic submodel

2.2.1. Magnetic field equations

The magnetic field was solved in the harmonic domain, specifying the current amplitude and frequency, assuming the coil current's periodicity. The time-harmonic equation for the magnetic field is solved with Maxwell-Ampère's law [35]:

$$\nabla \times \mathbf{H} = \mathbf{J} + j\omega_f \mathbf{D} \tag{1}$$

Where $\mathbf{H}$ is the magnetic field, $\mathbf{J}$ the current density, and $\mathbf{D}$ the electric displacement and ω_f is the angular frequency. Considering Ohm's law with the Lorentz term for the liquid metal flow $\mathbf{J} = \sigma\mathbf{E} + \sigma(\mathbf{u} \times \mathbf{B}) + \mathbf{J}_\mathrm{e}$ it can be rewritten as:

$$\nabla \times \mathbf{H} = \sigma\mathbf{E} + \sigma(\mathbf{u} \times \mathbf{B}) + \mathbf{J}_\mathrm{e} + j\omega_f \mathbf{D} \tag{2}$$

where σ is the electrical conductivity, $\mathbf{E}$ the electrical field,$\mathbf{u}$ the melt flow velocity vector and $\mathbf{J_e}$ the current density source. Introducing the field potentials $\mathrm{B} = \nabla \times \mathrm{A}$ and $\mathbf{E} = -j\omega\mathbf{A}$ and the constitutive relations $\mathbf{B} = \mu_0\mu_\mathrm{r} \times \mathbf{H}$ and $\mathbf{D} = \varepsilon_0\varepsilon_\mathrm{r} \times \mathbf{E}$ it can be derived the resulting partial differential equation (PDE) solved for the magneto-hydrodynamic submodel.

$$\mathbf{J} = \left(j\omega_\mathrm{f}\sigma - \omega_f^2\varepsilon_0^{-1}\varepsilon_\mathrm{r}^{-1}\right)\mathbf{A} + \nabla \times \left(\mu_0^{-1}\mu_\mathrm{r}^{-1}\nabla \times \mathbf{A}\right) - \sigma\mathbf{u} \times (\nabla \times \mathbf{A}) + \mathbf{J_e} \tag{3}$$

where, μ^{-1} is the magnetic permeability and ε electrical permittivity. The magnetic vector potential $\mathbf{A}$ is necessary for the resolution of the fields according to the $\mathbf{A}$ formulation satisfying the magnetic Gauss' law $\nabla \times \mathbf{B} = 0$ as $\nabla \cdot \nabla \times \mathbf{A} = 0$ always holds.

The external current density $\mathbf{J_e}$ was determined by the input power of the coil fed by the power generator. The coil was modeled by the coiling functionality of COMSOL Multiphysics® being a single conductor, a solid region through which the current passes. Although each turn of the coil is considered a separate domain, they are treated as a coil group to facilitate the connection between the solenoid loops. The external current density, $\mathbf{J_e}$, is determined by taking into account the out-of-plane component of the current I_C.

$$\mathbf{J_e} = \frac{\sigma V_C}{2\pi\mathrm{r}} \tag{4}$$

The V_c potential can be obtained by constraining the total integrated current to I_C. The current density and the voltage within the coil determine the excitation power of the coil. The input power introduces an additional constraint and a non-linearity in the equations requiring specifying the phase angle between the two vectors. It is important to note that

the model was fed with the experimentally measured current and voltage variables. Thus, the coil imposed power excitation P_{C}, introducing the following additional constraint and the phase shift between the current and voltage $\cos(\varphi)$:

$$P_{\mathrm{C}} = \frac{1}{2}\Re\mathrm{e}(V_C \cdot I_C^* \cdot \cos(\varphi)) \tag{5}$$

2.2.2. Hydrodynamic equations

The magnetic field induces two related effects on the flow of the liquid metal: the free surface deformation and the generation of a turbulent recirculating stirring. The Navier-Stokes equations govern the momentum transport, which in the time domain for an incompressible Newtonian flow and considering the conservation of mass and momentum are written as [36]:

$$\frac{\partial \rho}{\partial \mathrm{t}} + \nabla \cdot (\rho \mathbf{u}) = 0 \tag{6}$$

$$\rho\left(\frac{\partial \mathbf{u}}{\partial \mathrm{t}} + \mathbf{u} \cdot \nabla \mathbf{u}\right) = -\nabla p + \nabla \cdot \mathbf{K} + \rho \mathbf{g} + \mathbf{F_L} + \mathbf{F_{ST}} \tag{7}$$

where $\mathbf{u}$ is the flow velocity, ρ the fluid density, p is the pressure, $\mathbf{K}$ corresponds to the stress tensor $\mathbf{K} = (\mu + \mu_T)\left(\nabla \mathbf{u} + (\nabla \mathbf{u})^{\mathrm{T}}\right)$, μ dynamic viscosity, μ_T turbulent viscosity or eddy viscosity, $\mathbf{F_L}$ is the Lorentz force, $\mathbf{F_{ST}}$ surface tension, and $\mathbf{g}$ the gravitational force.

To calculate the mean flow of the turbulent fluid flow field $\mathbf{u}$; the standard $k-\varepsilon$ RANS model was employed with wall function approximation to compute the sub-viscous layer flow velocity. It was considered an acceptable option as a first approximation, providing an easier convergence due to wall functions and relatively good results for the demanded computational cost. Two additional dependent variables corresponding to the turbulent kinetic energy (k) and the turbulent dissipation rate (ε) and a transport equation for each were included [36], the transport equations for k read:

$$\rho\frac{\partial k}{\partial \mathrm{t}} + \rho \mathbf{u} \cdot \nabla k = \nabla \cdot \left(\left(\mu + \frac{\mu_T}{\sigma_k}\right)\nabla k\right) + \mathrm{P}_k - \rho\varepsilon \tag{8}$$

And the transport equation of ε reads:

$$\rho\frac{\partial \varepsilon}{\partial \mathrm{t}} + \rho \mathbf{u} \cdot \nabla \varepsilon = \nabla \cdot \left(\left(\mu + \frac{\mu_{\mathrm{T}}}{\sigma_\varepsilon}\right)\nabla \varepsilon\right) + C_{\varepsilon 1}\frac{\varepsilon}{k}\mathrm{P}_k - C_{\varepsilon 2}\rho\frac{\varepsilon^2}{k} \tag{9}$$

While the turbulent production rate P_{k} is defined as:

$$P_k = \mu_T\left(\left(\nabla \mathbf{u} : (\nabla \mathbf{u} + \nabla \mathbf{u}^T)\right)\right) \tag{10}$$

The turbulent viscosity (μ_T) is derived from k and ε with the expression:

$$\mu_T = \rho C_\mu \frac{k^2}{\varepsilon} \tag{11}$$

The constants σ_{k}, σ_ε, $\mathrm{C}_{\varepsilon 1}$, $\mathrm{C}_{\varepsilon 1}$and C_μ are the standard values of $k-\varepsilon$ formulation [36].

$$\sigma_k = 1.0\ ;\ \sigma_\varepsilon = 1.3\ ;\ C_{\varepsilon 1} = 1.44\ ;\ C_{\varepsilon 2} = 1.92\ ;\ C_\mu = 0.09 \tag{12}$$

The source term that induces flow movement is the magnetic or Lorentz force. This force induces a mechanical momentum in the flow and magnetic pressure in the radial direction to the crucible axis, pushing the melt away from the crucible wall inwards. It can

be described as the vectorial product between the magnetic field and the induced current in the electrically conducting medium [35].

$$\mathbf{F_L} = \frac{1}{2}\Re\mathrm{e}(\mathbf{J} \times \mathbf{B}^*) \tag{13}$$

The hydrostatic force calculation is straightforward as it is the product of the volume force generated by gravity $\rho\mathbf{g}$. Finally, the surface tension force $\mathbf{F_{ST}}$ it is related to the surface gradient operator $\nabla_s = \left(\mathbf{I} - \mathbf{n_i}\mathbf{n_i}^{\mathbf{T}}\right)$, being $\mathbf{I}$ the identity matrix, $\mathbf{n_i}$ the normal of the interface and γ, the surface tension in the free surface following the expression [37]:

$$\mathbf{F_{ST}} = \gamma(\nabla_s \cdot \mathbf{n_i})\mathbf{n_i} - \nabla_s\gamma \tag{14}$$

2.2.3. Moving mesh

After defining all forces acting in the liquid metal, the need to find the displacement of the metal fluid free surface led to the moving mesh method. This method, employing the Arbitrary Lagrangian-Eulerian (ALE) approach, accurately tracked the moving boundary by allowing mesh nodes to follow the fluid flow. ALE combined Eulerian and Lagrangian advantages, solving fluid equations for $\mathbf{u}$ and p fields in a moving reference frame with mesh displacement.

Free mesh normal direction deformation was enabled in the domain corresponding to the liquid metal, and free mesh slips to the metal-crucible wall boundary to allow the tangential displacement. PDEs for the mesh displacement were solved to ensure a smooth mesh deformation and the propagation of the moving domain displacement; in this case, the Winslow method was adopted as a smoothing algorithm deemed suitable for unstructured meshes. A moving mesh control was used to address potential distortions from moving mesh methods, updating nodes iteratively to maintain numerical stability. If any mesh element quality fell below 0.2, a remeshing operation was triggered to ensure convergence and stability in the numerical calculation. Once the mesh was remeshed, the simulation resumed from the previous state.

2.2.4. Boundary conditions

The boundary conditions were tailored to address the fluid flow field, turbulent variables, and mesh displacement, summarized in Table 1.

Table 1. Boundary conditions for the hydrodynamic and moving mesh model.

Boundary	Physical interface		
	Flow field ($\mathbf{u}$)	Turbulence (k/ε)	Moving Mesh
Wall (Nº 4)	$\mathbf{u} \cdot \mathbf{n} = 0$ $\mathbf{K} \cdot \mathbf{n} = -\rho\frac{\mathrm{u_K}}{\mathrm{u^+}}\mathbf{u}_{\mathrm{tang}}$	$\nabla k \cdot \mathbf{n} = 0$ $\varepsilon = \frac{C_\mu^{3/4}k^{3/2}}{\mathrm{k_v}\delta_\mathrm{w}^+}$	$\mathbf{u}_{\mathrm{tang}} = \mathbf{u} - (\mathbf{u} \cdot \mathbf{n})\mathbf{n}$ $\mathrm{d_r} = 0$
Fluid-Fluid Interface (Nº 3)	$\mathbf{u}_1 = \mathbf{u}_2$ $\mathbf{n}_i \cdot \mathbf{K}_2 = \mathbf{n}_i \cdot \mathbf{K}_1 + \mathbf{F_{ST}}$	-	$\mathbf{u}_{\mathrm{mesh}} \cdot \mathbf{n}_i = \mathbf{u} \cdot \mathbf{n}_i$
Open Boundary (Nº 5)	$\mathbf{K} \cdot \mathbf{n} = 0$	$\nabla k \cdot \mathbf{n} = 0$ $\nabla\varepsilon \cdot \mathbf{n} = 0$	$\mathrm{d_r} = 0$; $\mathrm{d_z} = 0$

For coupling the flow field with the moving mesh interface, a tangential velocity field $\mathbf{u}_{\mathrm{tang}}$ was introduced to link mesh deformation and fluid wall velocity, modifying the boundary condition $\mathbf{u} = 0$ to a no-slip condition $\mathbf{u} \cdot \mathbf{n} = 0$. The mesh displacement in the radial

direction was fixed, imposing the displacement of zero $\mathrm{d_r} = 0$. The standard wall function was implemented to account for turbulence effects (k and ε) near the wall in function to the wall lift-off (δ_w^+) and the von Kármán constant ($\mathrm{k_v}$), details of the implementation can be found elsewhere [38]. The velocity profile in this region approximated a logarithmic function relating to turbulence variables based on the distance from the wall y^+, introducing the friction velocity $\mathbf{u}_K$ and the non-dimensional velocity $\mathbf{u}^+$ [36].

A fluid-fluid interface condition was applied to handle mesh displacement at the interface boundary between air and liquid metal and ensure accurate flow resolution. This condition enforced equal velocities between the two sides of the interface $\mathbf{u_1} = \mathbf{u}_2$ with no mass transfer across the boundary and the mesh velocity at the interface $\mathbf{u}_{\mathrm{mesh}}$. The viscous stress tensor $\mathbf{K}$ of the two domains related to the interface's normal vector $\mathbf{n}$ while accounting for surface tension $\mathbf{F}_{\mathrm{ST}}$. This enabled the calculation of the interface velocity, equating it to the mesh displacement [37].

The crucible top boundary was treated as an open boundary with no shear stress, assuming zero turbulent kinematic energy and dissipation rate in this region. The mesh displacement on the open boundary was fixed $\mathrm{d_r} = \mathrm{d_z} = 0$ to ensure mass conservation.

For the magnetic field, the unique necessary boundary condition was the close of the magnetic loop with the magnetic insulation boundary condition in the vacuum chamber's inner boundary $\mathbf{n} \times \mathbf{A} = 0$.

2.3 Magneto-thermo-hydrodynamic model

The second effect of the magnetic field is the induction heating effect due to the dissipation of the eddy currents that, for an alternating magnetic field, is related to the electrical conductivity and the product of electrical tension and current density [35]:

$$\boldsymbol{Q}_{\mathbf{e}} = \frac{1}{2}\Re\mathrm{e}(\mathbf{J} \cdot \mathbf{E}^*) \tag{15}$$

where $\boldsymbol{Q}_e$ is the heat generated and acts as a source term for the heat equation.

2.3.1. Thermal field equations

The energy equation was incorporated into the magneto-hydrodynamic model presented and considered the effect of the turbulent heat transfer. Natural convection effects induced by temperature differences were disregarded because of the higher effect of magnetic heating. The heat transfer equation solved in the melt can be written as [39]:

$$\rho \mathrm{C_p}\left(\frac{\partial T}{\partial \mathrm{t}} + (\mathbf{u} \cdot \nabla T)\right) = \nabla \cdot (\lambda_{\mathrm{eff}} \nabla T) + \boldsymbol{Q_e} \tag{16}$$

Where T is the temperature field, $\mathrm{C_p}$ is the specific heat capacity, and the factor λ_{eff} is the sum of the contribution of the liquid metal thermal conductivity λ and the turbulent thermal conductivity λ_{T}, which takes into account the enhanced heat transfer due to turbulent mixing depending on the flow conditions and the turbulent viscosity:

$$\lambda_T = \mu_T \, {\mathrm{C_p}}/{\mathrm{Pr_T}} \tag{17}$$

Therefore, the fluid flow and temperature fields have to be coupled; a non-isothermal approach was considered by introducing the turbulent Prandtl number Pr_T that relates to the momentum and heat transfer of turbulent diffusion. The turbulent Prandtl number $\mathrm{Pr_T}$

is derived from the Extended Kays-Crawford model [40], which relates the turbulent flow and the heat transfer in the boundary layers.

2.3.2. Low Reynolds number model hydrodynamic equations

The standard $k-\varepsilon$ model mentioned above assumes a high Reynolds number, in the order of 10^5, resulting in fully developed turbulent flow and the need for wall functions to define velocity in the near-wall boundary layer. This can lead to an artificial increment of the velocity at the wall, distorting the convective heat transfer.

However, for the induction melting case, turbulence was calculated to be in the order of 10^4. A low Reynolds approach addresses these uncertainties, resolving turbulence equations through the buffer and viscous sublayer up to the wall. The Low Reynolds Number (LRN) $k-\varepsilon$ formulation enhances the previous standard $k-\varepsilon$ model by modifying the turbulence transport equations with nonlinear damping factors. Specifically, the AKN model has been implemented to couple efficiently with heat transfer [41]; the transport equations for, k and ε, including the damping function f_ε reads as:

$$\rho\frac{\partial k}{\partial t}+\rho\mathbf{u}\cdot\nabla k=\nabla\cdot\left(\left(\mu+\frac{\mu_T}{\sigma_k}\right)\nabla k\right)+P_k-\rho\varepsilon \tag{18}$$

$$\rho\frac{\partial \varepsilon}{\partial t}+\rho\mathbf{u}\cdot\nabla \varepsilon=\nabla\cdot\left(\left(\mu+\frac{\mu_T}{\sigma_\varepsilon}\right)\nabla \varepsilon\right)+C_{\varepsilon1}\frac{\varepsilon}{k}P_k-f_\varepsilon C_{\varepsilon2}\rho\frac{\varepsilon^2}{k} \tag{19}$$

Where the production rate P_k is written as:

$$P_k=\mu_T\left(\left(\nabla\mathbf{u}:(\nabla\mathbf{u}+\nabla\mathbf{u}^T)\right)\right) \tag{20}$$

For the turbulent viscosity model, the second damping function, f_μ,is included:

$$\mu_T=\rho f_\mu C_\mu\frac{k^2}{\varepsilon} \tag{21}$$

While the damping functions, f_μ and f_ε reads and additional functions are introduced:

$$f_\mu=\left(1-e^{-\frac{l^*}{14}}\right)^2\cdot\left(1+\frac{5}{R_t^{3/4}}e^{\left(-\frac{R_t}{200}\right)^2}\right) \tag{22}$$

$$f_\varepsilon=\left(1-e^{-\frac{l^*}{3.1}}\right)^2\cdot\left(1+0.3e^{\left(-\frac{R_t}{6.5}\right)^2}\right) \tag{23}$$

$$l^*=\frac{(\rho u_\varepsilon l_w)}{\mu};R_t=\frac{\rho k^2}{\mu\varepsilon};u_\varepsilon=\left(\frac{\mu\varepsilon}{\rho}\right)^{\frac{1}{4}} \tag{24}$$

where l_w corresponds to the closest wall distance, while the constants of the model are given by the AKN formulation [41]:

$$\sigma_k=1.4\,;\ \sigma_\varepsilon=1.4\,;\ C_{\varepsilon1}=1.5\,;\ C_{\varepsilon2}=1.92\,;\ C_\mu=0.09 \tag{25}$$

2.3.3. Boundary conditions

Accurately determining the heat fluxes across the walls, coupled with the high flow velocity gradients close to the walls, requires some modifications in treating the boundary conditions at the walls. Instead of wall functions, a low Reynolds approach was adopted for computing viscous and buffer layer flow. This wall treatment enforces a no-slip condition with zero velocity at the wall. The first mesh cell is included in the viscous

sublayer, requiring a finer mesh and improved quality. It is necessary to ensure that the distance between the wall and the first mesh element center is less than 1 in viscous units; thus, the first mesh element's length in the wall's vicinity was set at 0.5 mm.

For heat transfer analysis, two primary boundary conditions were taken into account: radiation ($\mathbf{q_{rad}}$) acting on the metal's exposed surface and forced convection ($\mathbf{q_{dis}}$) along the inner contour of the coil (Nº 7), facilitated by the coil's water cooling.

The radiation condition applies to the metal's free surface, considering the emissivity (ϵ), the Stefan-Boltzmann constant σ_{sb} and temperature difference between the free surface and the infinite reference T_∞, assumed to be 25 ºC. Forced convection at contour, Nº 7, depends on experimentally measured heat dissipation, influenced by inlet/outlet temperatures. Here, T_{ext} denotes the inlet water temperature of 20 ºC and heat transfer coefficient h, which is parametrized to adjust for measured heat losses due to crucible conduction $\mathbf{q}_{\mathrm{dis}}$.

The outer melt-box contour was treated as a thermal insulation boundary to provide thermal insulation. These boundary conditions should be considered in conjunction with the previously described fluid flow and turbulence-determining conditions. The summarized boundary conditions are presented in Table 2.

Table 2. Boundary conditions for the coupled thermo-hydrodynamic model.

Boundary	Description	Physical interface		
		Flow field ($\mathbf{u}$)	Turbulence (k/ε)	Temperature (T) Heat flux ($\mathbf{q}$)
Free Surface (N°3)	Radiation Surface	$\mathbf{K}\cdot\mathbf{n}=0$	-	$-\mathbf{n}\cdot\mathbf{q_{rad}}=\epsilon\cdot\sigma_{sb}(T_\infty^4-T^4)$
Internal Wall (N° 4)	No-slip	$\mathbf{u}=0$	$k=0$ $\varepsilon=2\frac{\mu}{\rho}\frac{k}{l_w^2}$	$-\mathbf{n}\cdot\mathbf{q}=-\lambda_{\mathrm{eff}}\nabla T$
Coil int. boundary (N° 7)	Forced Convection	-	-	$-\mathbf{n}\cdot\mathbf{q_{dis}}=h(T_{ext}-T)$
Crucible - Melt-box (N° 6)	Thermal Insulation	-	-	$-\mathbf{n}\cdot\mathbf{q}=0$

2.4 Meshing and solver configuration

The mesh definition is critical, especially when dealing with coupled nonlinear physical interfaces like flow transport and magnetic field. The meshing sequence was divided into two steps according to the goal of the simulations. As an initial step for the mesh deformation study, unstructured triangular mesh elements were employed, adjusting the minimum element size to capture the skin effect. The coil domains were meshed through the boundary layer mesh to capture the resistive losses due to the auto-inductance effects in the copper windings. For the rest of the domains, triangular mesh elements with extremely fine sizes were employed. During the moving mesh simulation, an automatic re-meshing algorithm improves calculation stability and avoids generating degenerated mesh elements. In each iteration, a mesh control was applied to verify that the element's minimum quality was over 0.2, and if not, the mesh elements were adapted to the actual deformation. An example of the mesh for the last time step can be seen in Fig. 3. a.

For the fluid recirculation simulation, a mesh refinement was performed to improve the quality of mesh elements and increase resolution, especially in the fluid-wall interface. The grid was adjusted iteratively to ensure computation convergence based on the relative error defined by the velocity gradient of the fluid flow (Fig. 3. b.).

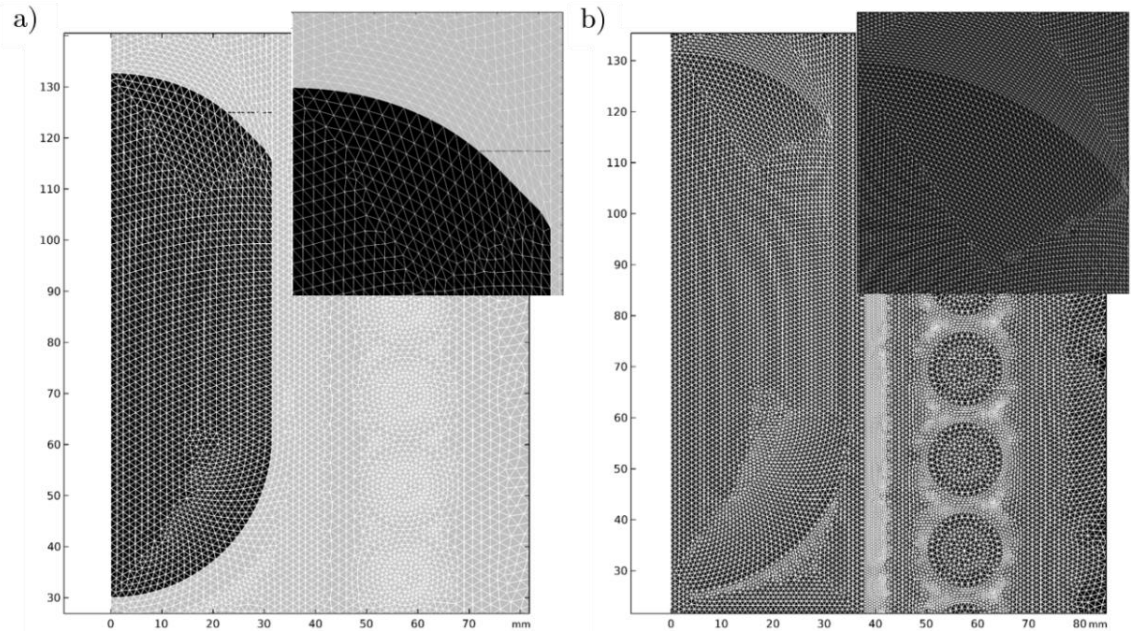

Fig. 3. a) Final mesh for deformation study. b) Refinement for flow stationary study.

Moreover, a mesh validation and sensitivity study was done to ensure the repeatability of the results, reducing the mesh maximum length size. Table 3 resumes the sensitivity of the mesh results from the LRN turbulence model; the magnetic field and Lorentz force results were consistent, thus, only the averaged and maximum velocity are presented.

Table 3. Mesh sensitivity analysis for fluid velocity field results at 8.3 kW applied power.

Max Lenght	N° Elements	Average Quality	$\mathbf{u}_{\mathrm{avg}}$ [m/s].	$\mathbf{u}_{\mathrm{max}}$ [m/s]
4	$1.2{\cdot}10^5$	0.92	12.8	33.0
2	$1.5{\cdot}10^5$	0.92	12.9	33.1
1	$2.5{\cdot}10^5$	0.92	12.9	33.3
0.5	$6.4{\cdot}10^5$	0.93	13.0	35.5

For the $\mathbf{u}$ and p fields, second-order (P2+P1) discretization was adopted, while for magnetic vector potential, quadratic elements were used. A segregated solver was employed to solve the fields, dividing the problem into various steps corresponding to each physics and computed sequentially in each iteration. This way, smaller equation matrixes were generated. However, more iterations were required to get a convergent solution. The time step was limited to 1 ms in the free surface study while for the heat transfer 1 second was established. All fields were resolved with the direct solvers integrated in COMSOL Multiphysics®.

2.5 Material properties

The material properties for the resolution of the above-presented equations are resumed in Table 4. Regarding electromagnetics, all materials have been considered paramagnetic $\mu_r = 1$ while the crucible and melt box are electrically insulators $\sigma = 0$. For

the coil's copper, the thermophysical and electrical material properties rely on the COMSOL Multiphysics® database. For the thermophysical and electrical properties of liquid Inconel 718, values reported by Mills [42] at 1500 °C are considered. Emissivity (ϵ) was estimated to be 0.2 according to the pyrometer calibration.

The alumina (Al_2O_3) crucible and melt-box concrete (Al_2O_3-CaO) thermal properties were characterized in the 25-1500°C and interpolated, which is implemented in the molde as a built-in function. Following the sapphire ratio method, the specific heat capacity Cp was determined with the differential scanning calorimetry (DSC Netzsch STA 449 F3 Jupiter®). For the thermal diffusivity laser flash analysis (LFA Linseis 1000®) technique was employed. Considering that refractories have a low thermal expansion coefficient, a constant bulk density was estimated by the relation of volume and mass. The thermal conductivity was characterized as the product of the density, thermal diffusivity, and specific heat capacity $\mathrm{k(T)} = \rho \cdot \alpha(\mathrm{T}) \cdot \mathrm{Cp(T)}$.

In addition to Inconel 718, aluminum was also employed as melting material in the open-air induction melting furnace. Consequently, the aluminum properties pertinent to the magneto-hydrodynamic model are included in the material properties Table 4 for a temperature of 750 ºC.

Table 4. Material properties for the implemented domains.

Material	Density $\rho\ \left(\frac{\mathrm{kg}}{\mathrm{m^3}}\right)$	Thermal Conductivity $\lambda\ (\frac{\mathrm{W}}{\mathrm{m \cdot K}})$	Heat capacity $\mathrm{C_p}\ \left(\frac{\mathrm{J}}{\mathrm{kg \cdot K}}\right)$	Electrical conductivity $\sigma\ \left(\frac{\mathrm{S}}{\mathrm{m}}\right)$	Dynamic Viscosity $\mu\ \left(\frac{\mathrm{kg}}{\mathrm{m \cdot s}}\right)$	Surface Tension $\gamma\ (\mathrm{N \cdot m})$
Inconel 718 [42]	7400	29.6	720	$6.67 \cdot 10^5$	$5.4 \cdot 10^{-3}$	1.86
Aluminum [44]	2300	-	-	$3.6 \cdot 10^5$	$1.29 \cdot 10^3$	0.85
Al_2O_3	2950	$-1.72 \cdot \ln(T)+17.3$	$0.32 \cdot T^{0.187}$	0	-	-
Al_2O_3-CaO	2730	$-0.52 \cdot \ln(T)+6.11$	$0.29 \cdot T^{0.239}$	0	-	-
Copper	8960	400	385	$6e^7$	-	-

3. Experimental measurements

Experimental tests were conducted to provide references for feeding the numerical model and subsequent comparison and validation. The study focused on two critical aspects of induction melting. Firstly, the free surface deformation was examined to validate the magnetic-hydrodynamic coupling. Secondly, the transient response to power changes and resulting metal temperature adjustment were analyzed to validate the temperature field coupling.

3.1 VIM experimental set-up

Before the melting trials, the VIM installation was set to acquire the required process variables to implement the previously described model. A specific set-up was developed for the data acquisition, employing a 16-channel National Instruments NI-9207® module as analog inputs recording at 1 Hz sample frequency. The recorded signal data were thermocouple and pyrometer temperature, induced power data; heat dissipated on the water-cooled coil, and vacuum chamber pressure. All the data was imported to an in-house developed real-time monitoring system for the melting process variables control and measurement for the posterior data analysis.

Regarding the measured temperature variations during the trials, an Optris CTRatio_1MH dual-wavelength pyrometer was employed to measure the top surface temperature of the metal, with a measuring range between 700 °C and 1800 °C. This was placed outside the vacuum chamber, aiming the metal top surface from a viewport. Before the data recording, the pyrometer was calibrated with an immersion B-type thermocouple. Additionally, a sensorized crucible (Fig. 4) was fabricated to measure the thermal response of the melt to applied power variations. This device consisted of an Al_2O_3 crucible with two K-type thermocouples attached, one at the base of the crucible (TC_1) and the second on the vertical wall (TC_2). Before the trials, it was verified that the magnetic field did not affect the thermocouple reading.

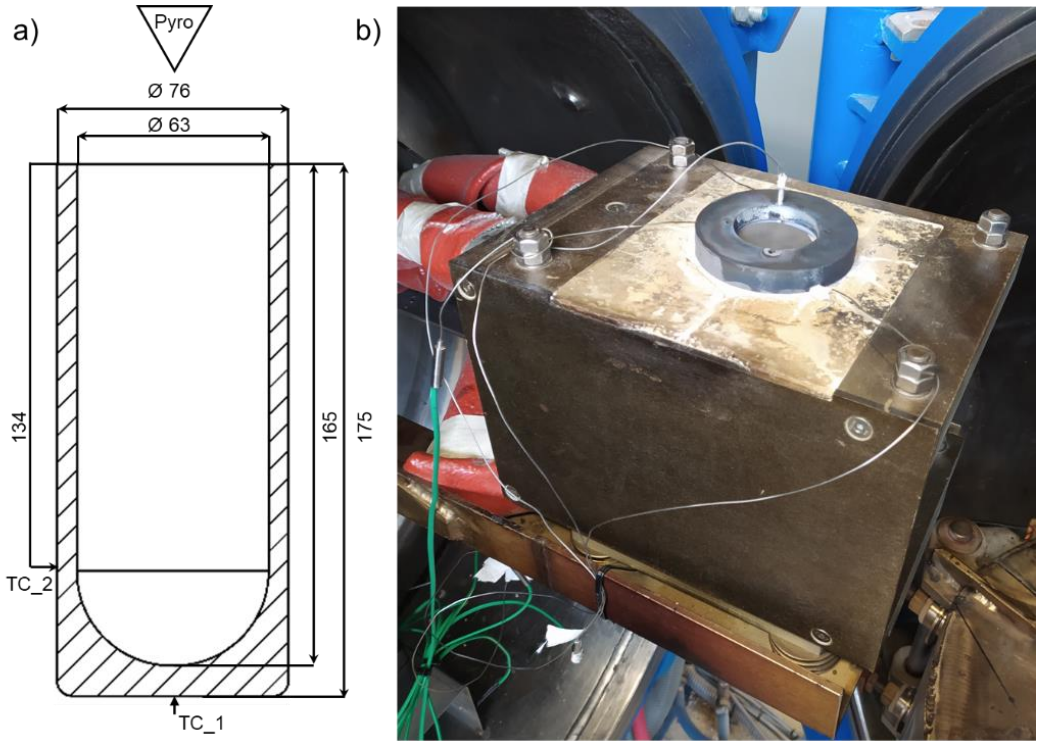

Fig. 4. a) Crucible section and thermocouple position. b) Melt-box configuration.

The heat dissipated in the refrigerated coil via conduction through the crucible and melt box was derived from the calorimetric balance method $\mathbf{q}_{\mathrm{dis}} = \dot{m}C_p\Delta T$ [43]. For that, the coil refrigeration was controlled with a water flow sensor and two temperature resistance detectors were placed in the inlet and outlet to measure the temperature variation.

A closed-loop ASIC-based Hall Effect LEM LF-2010-S® current transducer was employed, connected in series with the coil and power generator. Regarding the voltage, a LEM AV 100-750® voltage transducer was connected in parallel to the coaxial port entrance as close as possible to the coil. The analog output signal was conditioned to adapt to the resolution of the NI-9207 data acquisition system. A YOKOGAWA DLM 2024® oscilloscope was employed to visualize the waveform amplitude and frequency.

3.2 Melting trial and data acquisition

The objective of the melting trial was the transient measurement of the temperature of both the melt and crucible throughout the melting process. The trial followed a standard melting procedure involving two quasi-stationary stages to adjust the melt temperature. A stepped power application procedure was utilized to heat the charge. Once the charge had completely melted, the coil power was adjusted to reach the target temperature of

1500 °C and maintained for 10 minutes. Then it was followed by a transition stage, during which the coil power was reduced, and the temperature gradually decreased to 1450 °C, holding steady for 15 minutes (Fig. 5). It is important to note that maintaining a constant power did not result in a stable stationary temperature state due to the low thermal inertia of the melt, leading to rapid temperature variations. Therefore, slight power adjustments were necessary to sustain the target temperature.

During the trial, it was observed that the lower side thermocouple TC_1 exhibited higher thermal inertia compared to the vertical thermocouple TC_2, which displayed a faster response and registered a temperature approximately 25 °C higher. This difference was expected since TC_2 was placed closer to the melt and, therefore, more sensitive to temperature fluctuations. These temperature stabilization stages served as reference points for the subsequent numerical model validation. The measured heat dissipation rate for the analyzed section is presented in Table 5. The chiller utilized an on-off mode of operation, resulting in a maximum variable temperature difference ΔT of 4-8 °C.

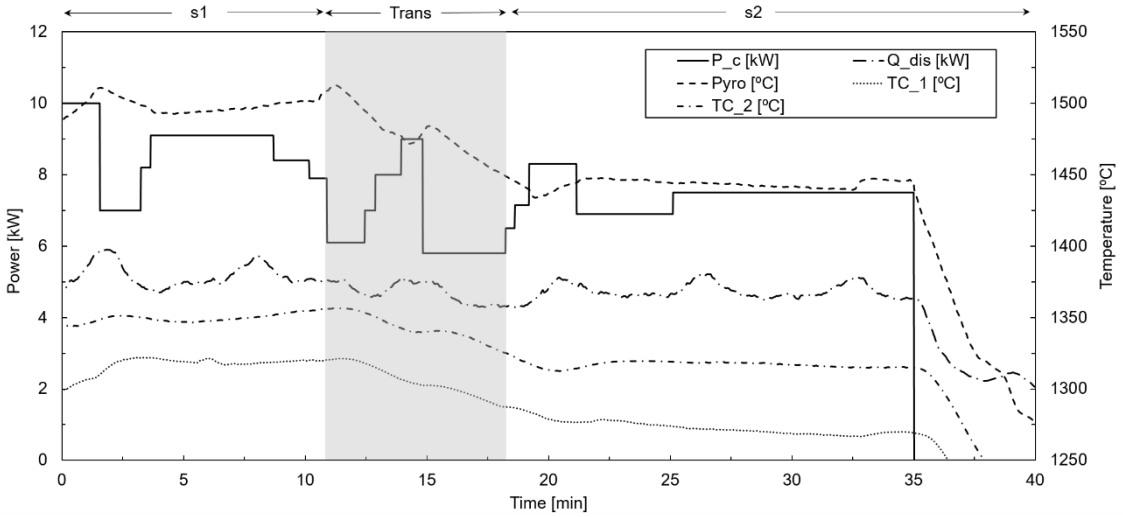

Fig. 5. Power-temperature-time of melting trial in quasi-stationary stages.

The analysis of the obtained experimental data is summarized in Table 5. The data for the two quasi-stationary stages with target temperature and corresponding duration, applied power, dissipating heat, and the transition stage. These references are input data for numerical simulations, posterior correlation, and validation purposes.

Table 5. Experimental trial stages, time steps, and process data.

Stage	Start	End	Duration [min]	P_c [kW]	q_{dis} [kW]	Temp [°C]
S-1	0	11	11	8.3	5.2	1500
Trans.	11	18.5	7.5	6.8	4.4	Variable
S-2	18.5	35	16.5	7.4	4.7	1450

For the above-measured power stages, the electrical variables of the coil were measured and later introduced as input in the numerical model. The measurements for different power stages corresponding to the root-mean square (RMS) current (I_c), voltage (V_c), frequency (f_c) and phase shift angle (φ) results are presented in Table 6.

Table 6. Measured electrical variables for input power.

Stage	P_c [kW]	I_c [A]	V_c [V]	f_c [kHz]	φ [deg]
S-1	8.3	915	138	7.4	86
Trans.	6.8	810	90	8.6	85
S-2	7.4	850	105	8.3	85

3.3 Open-air induction melting furnace

However, the challenges of working with high melting temperatures above 1350 °C in a vacuum chamber with limited space, no visible light, and magnetic fields make it difficult to acquire in-situ experimental data for the free surface shape. As a result, completing experimental trials and validating the numerical model for VIM presents technical difficulties. An alternative approach is employed to overcome these challenges using an air-open induction melting furnace (Fig. 6).

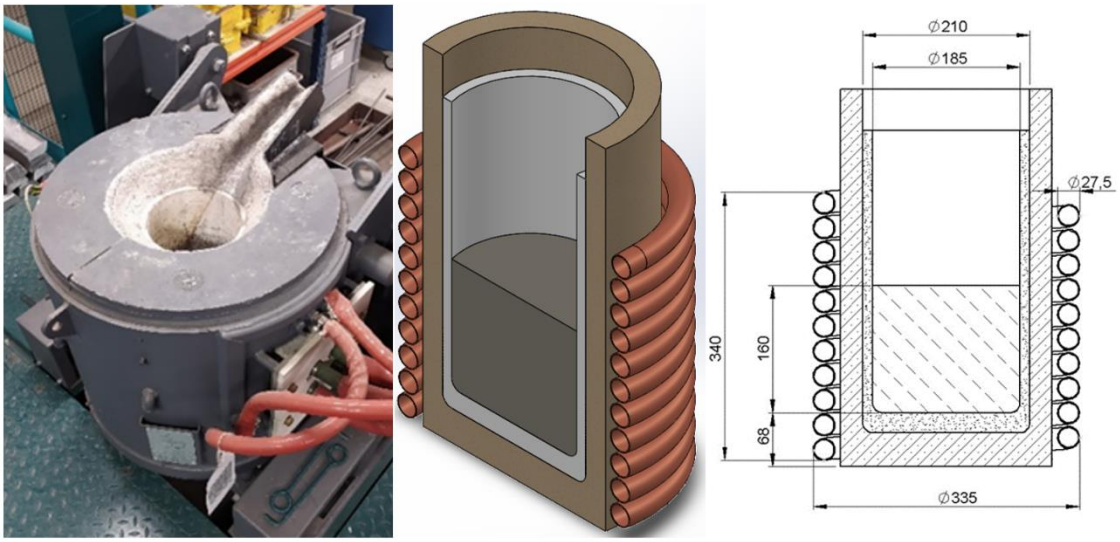

Fig. 6. Open-air induction melting furnace depict and dimensions.

The Inductotherm® Small Steel Shell furnace with a VIP Power-Trak+® power generator provides melting variables similar to industrial capacities, rated at 50 kW and 3 kHz. The larger dimensions of this furnace allow the melting of 20 kg of aluminum or 7.5 dm^3, making it more suitable for hydrodynamic studies.

The open-air furnace configuration offers several advantages, including easier melting processes, the possibility of installing acquisition systems, and the ability to observe the process with the naked eye. These benefits facilitate hydrodynamic model validation.

3.4 Free surface shape measurement

The aluminum underwent gradual heating with stepped power stages. Once the metal reached a fully liquid state, the temperature was elevated to approximately 750 °C and measured using a type K thermocouple. The presence of oxide particles was minimal in all the trials, and the few were concentrated in the wall crucible wall. The power was maintained at a fixed level to stabilize the temperature. A device consisting of 9 threaded rods was introduced into the metal's free surface to study the melt deformation. After wetting the rods for a few seconds, the device was carefully removed, leaving a mark

indicating the melt height and free surface profile. Three trials were conducted for different charge weights, corresponding to 5 kg, 7.5 kg, and 10 kg at fixed 25 kW of applied power. The melt deformation was assessed using contact probes, and the average height and relative error are shown in Fig. 7.

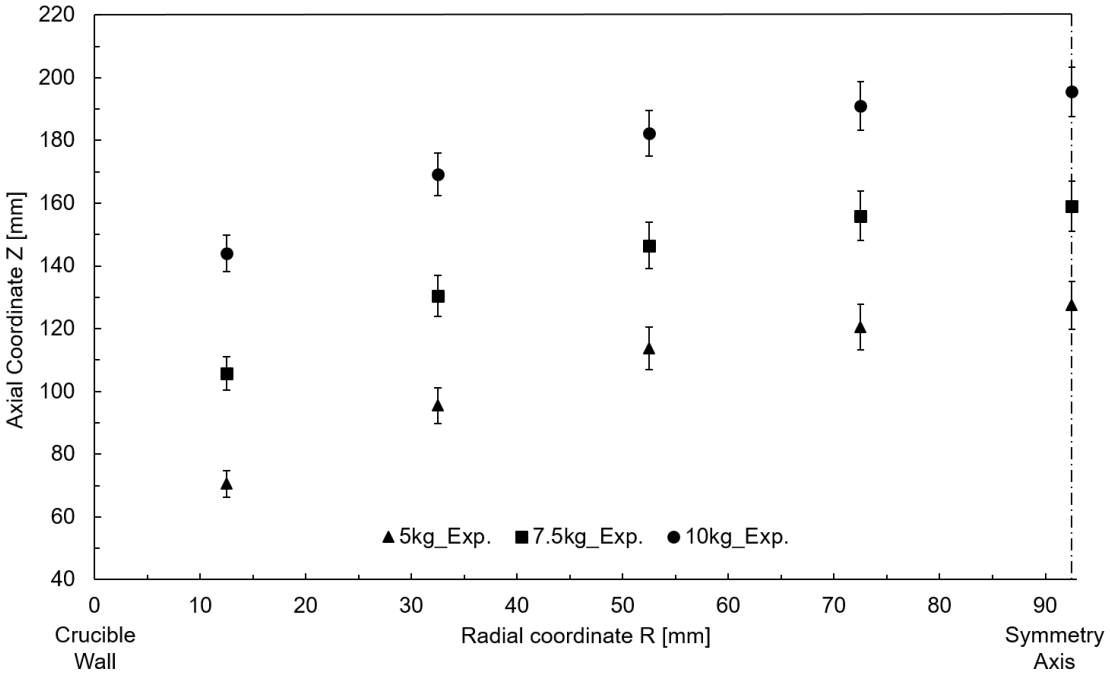

Fig. 7. Measured surface profile for 5, 7.5, and 10 kg mass-filling.

The results consistently showed a characteristic meniscus shape, with the initial height of the melt varying based on the crucible's mass filling. Trials with lower filling levels exhibited greater melt height and a more significant difference in height between boundary points. The measured electrical variables of the power unit that will serve as input for the simulation are summarized in Table 7.

Table 7. Resume of conducted test and electrical variables .

Mass [kg]	P_c [kW]	I_c [A]	V_c [V]	f_c [kHz]	φ [deg]
5	25	511	538	2816	83
7.5	25	514	541	2820	83
10	25	483	478	2916	84

4. Results and discussion

The model is studied under transient dynamic conditions for numerical results validation purposes according to the VIM experimental trial. The two quasi-stationary temperature stages are simulated by incorporating a transient adjustment stage. The obtained experimental data, summarized in Table 5 and Table 6, were incorporated into the model. The simulation procedure followed is depicted in Fig. 8.

The procedure begins with computing the magneto-hydrodynamic submodel trough the moving mesh method until a stationary profile is achieved. Subsequently, the mesh was refined to ensure an accurate solution for the flow velocity field, and the thermal model was coupled while maintaining the fixed free surface profile proceeding to the magneto-thermo-hydrodynamic submodel study.

After confirming the convergence of the calculations, the transient study was conducted until the end of the stage. When changes in the applied power, the simulation was paused by decoupling the thermal model and recalculating the new stationary free surface. The same approach was followed for the second quasi-steady state.

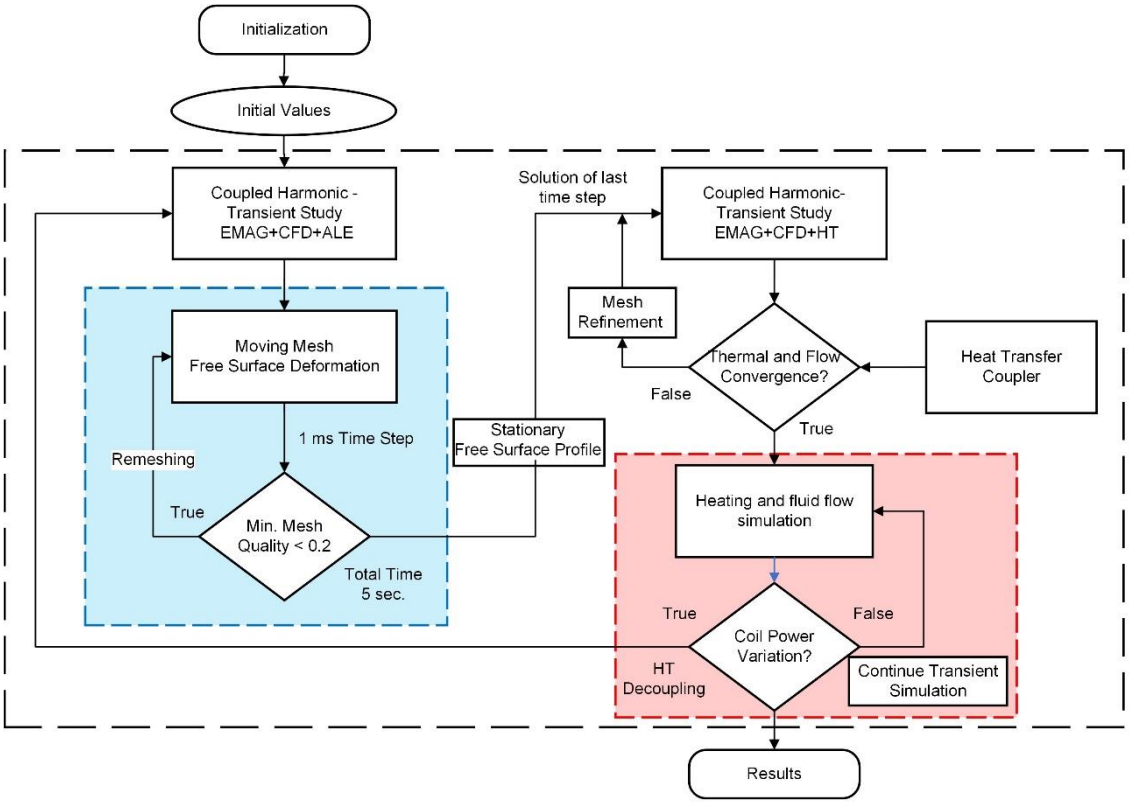

Fig. 8. Flow chart of the simulation procedure.

4.1 Magneto-hydrodynamic results

Before presenting the results for the VIM furnace, the ones for the open-air furnace are presented and discussed as they will serve as magneto-hydrodynamic submodel validation purposes.

4.1.1. Open-air IM free surface validation

Open-air induction melting surface deformation data was used to validate the free surface deformation profile. The mesh deformation model was adapted to the open-air IM furnace's geometry and operating electrical parameters. As mentioned previously, the heat transfer effects are neglected for the magneto-hydrodynamic model, studying solely the magnetic fields and hydrodynamics coupling. The implemented equations were detailed in Section 2.2 and boundary conditions of Table 1. A coupled frequency-transient mesh deformation was simulated for 5 seconds with a fixed time step of 5 ms, using a power ramp-up function for convergence assurance. Simulations were conducted for three mass filling levels, adapting the initial filling level to the mass and corresponding power input electrical variables, resumed in Table 7, and material properties of aluminum presented in Table 4 assuming a fixed homogeneous temperature of 750 ºC in the melt.

Fig. 9 depicts the computed surface profile for each simulation case after reaching a quasi-stationary situation, maintaining a stable maximum melt height. The numerical

results effectively captured the curvature profile formed by the point coordinate measurements, exhibiting a close replication. An increase in surface profile roughness was observed in the vicinity of the wall, particularly for the 5 kg filling case and between the wall and the first measurement reference. The low filling level generates a substantial magnetic force on the free surface border, resulting in pronounced distortion and rotation of the mesh elements.

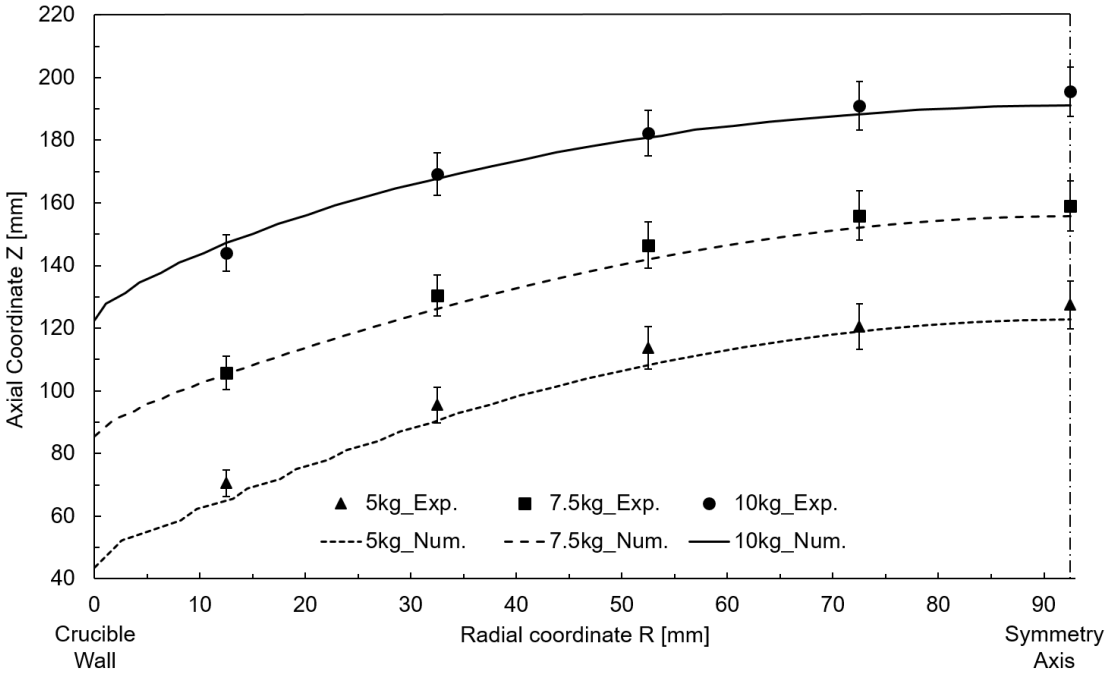

Fig. 9. Experimental and numerical correlation of the free surface profile.

4.1.2. VIM free surface analysis

Once stated the validity of the magneto-hydrodynamic model, the VIM case was studied. The coupled frequency-transient study has been launched with a 1 ms time step for a 5-second simulation with the input electrical variables corresponding to the 7.4 kW power stage. The implemented model electrical variables are based on the experimental measurements in Table 6. Fig. 10 depicts the maximum and minimum height of the melt in the axial coordinate for 2 seconds of simulation and the corresponding coil power.

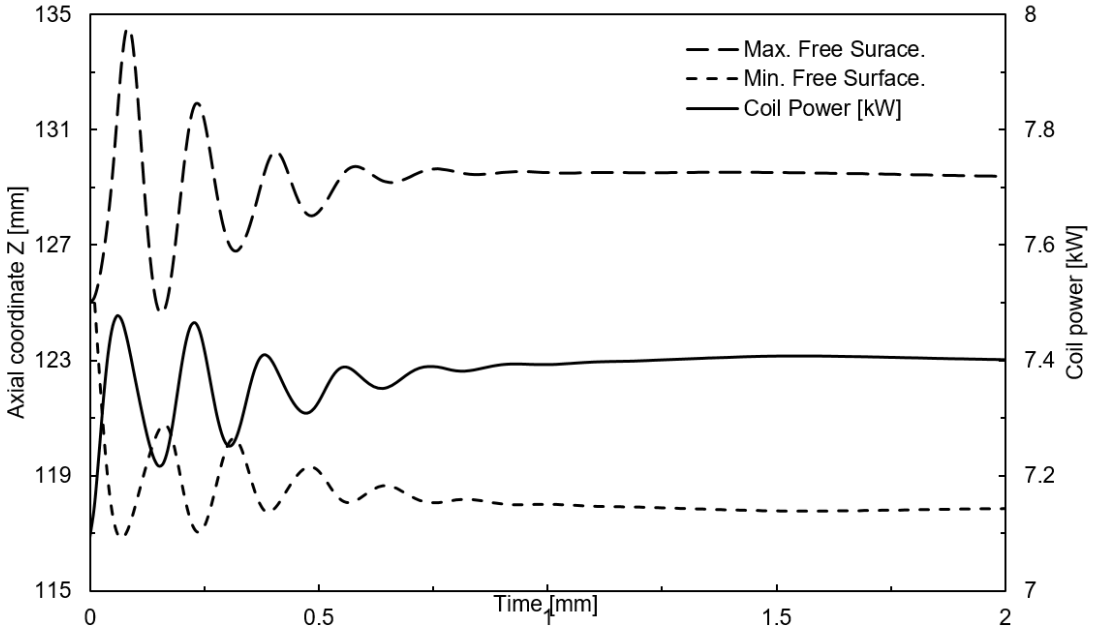

Fig. 10. Hydrodynamic free surface behavior for 7.4 kW power.

Initially, rapid oscillations of the free surface were observed, achieving an almost quasi-stationary state after almost 1-second. The coupling between fluid flow and magnetic fields evidences the parallelism between the free surface and coil power oscillations, evidencing that the deformation of the melt leads to a modification of the original magnetic field produced by the coil, and in the counter back, it affects the coil power.

The rapid variations might be related to the sudden application of the power and were not detected during the experimental trials. The reason arises from the generator's progressive power increment; thus, the deformation of the free surface is steadier without the computed transient fluctuations. Moreover, these rapid oscillations increase the computational cost as the mesh deformation increases, requiring remeshings steps. Thus a 1 s duration ramp-up step function was included in the coil power application to consider the progressive increment of the magnetic force, facilitating the convergence.

This power ramp-up modification simulated the free surface profile for the VIM coil and the two experimental quasi-stationary melting power stages. Similar results were obtained for both cases (Fig. 11), with a maximum height difference of 13 mm for 8.3 kW. This relatively small deformation results from the high hydrostatic pressure and the relatively low induced powers.

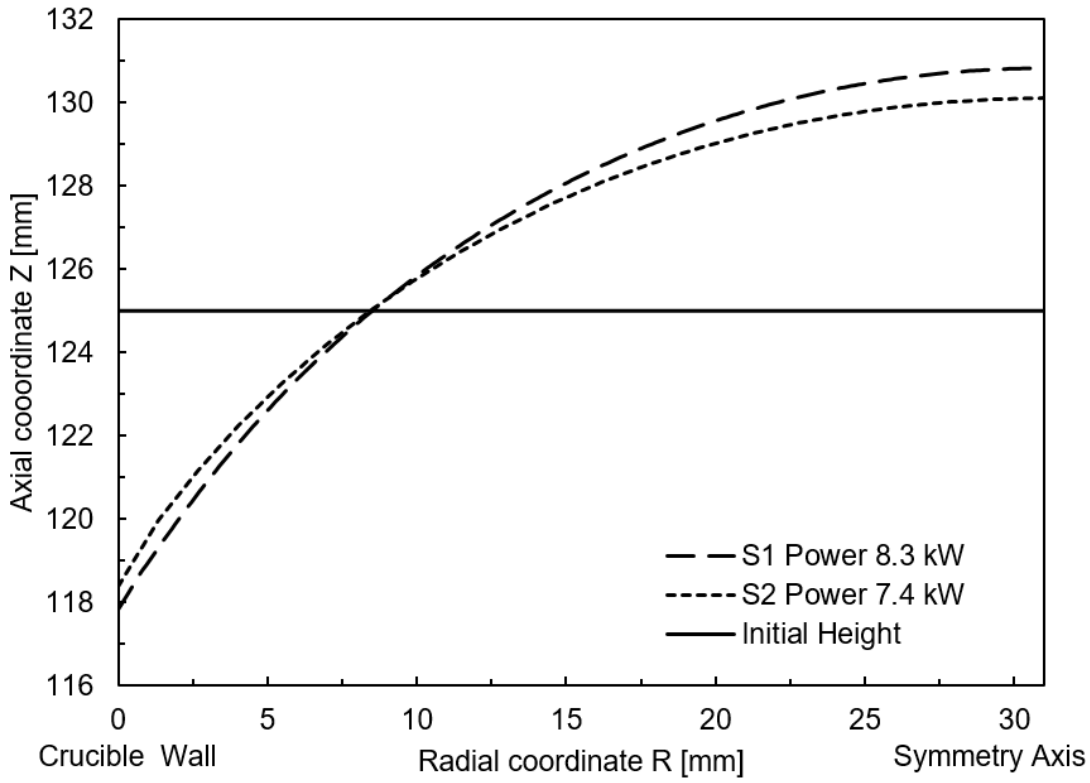

Fig. 11. Quasi-stationary free surface profile.

4.2 Magneto-thermo-hydrodynamic results

4.2.1. Magnetics field and flow field recirculation analysis

Fig. 12.a. illustrates the magnetic flux density and Lorentz force vectors within the liquid metal. The magnetic flux density was approximately 0.1 T, a typical value for this type of induction application. Lorentz force vectors were concentrated in the interface region, and the magnitude decreased while advancing into the metal. Coil excitation frequencies in the order of kHz concentrate the skin effect in a layer of 7 mm. This magnetic field concentration in the crucible-melt interface suggests localized heating in the film layer. This evidences that precise and fine meshing in the walls is essential to capture the heat convection and conduction effects between the melt and the crucible. For the power stage of 8.3 kW, a slightly higher magnetic field intensity of up to 0.12 T was computed while maintaining the same distribution.

Regarding the fluid velocity plotted in Fig. 12.b, the interaction between the magnetic pressure and hydrostatic normal forces resulted in a distinct recirculation pattern. Two main toroidal flows recirculated in opposite directions. The highest flow velocities were observed in the lower zone, near the curved wall of the crucible. Conversely, the velocity was nearly zero on the top surface, the vortices' center, and the stagnant points between the primary eddies. The magnitude of the velocity is in the range of 30 cm/s, in line with the previous numerical results reported in the bibliography for Wood's alloy [11] aluminum [30] and titanium [32] melting.

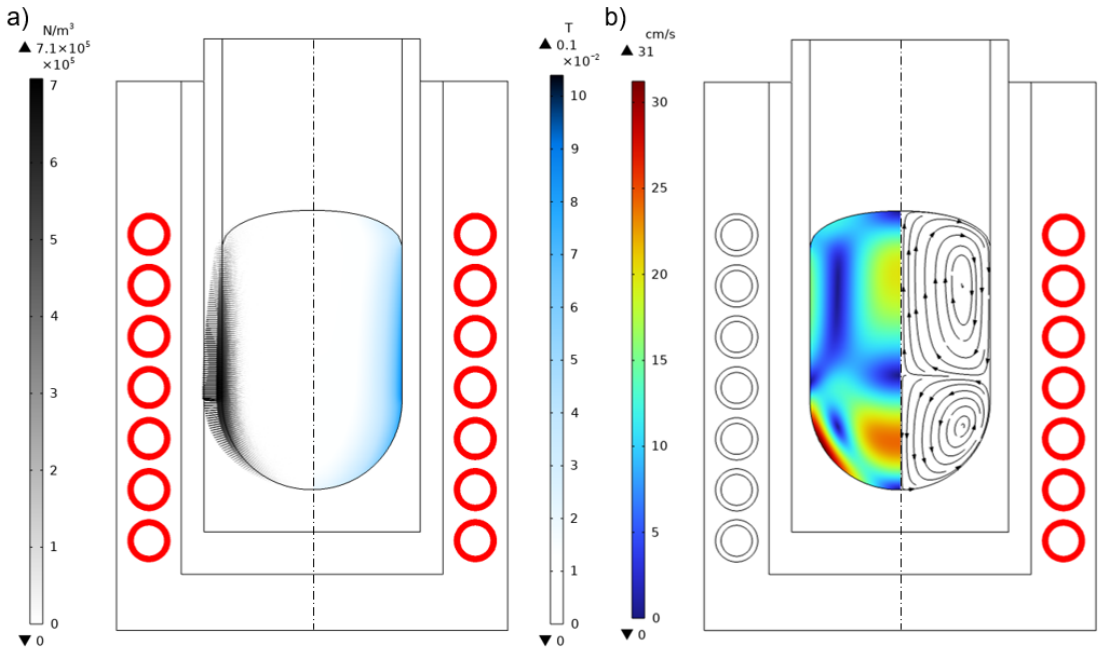

Fig. 12. For 7.4 kW input power. a) Lorentz force vectors and magnetic flux density. b) Velocity field and fluid pattern.

4.2.2. Temperature field analysis

The equations employed were described in Section 2.3, and boundary conditions correspond to Table 2. The model was initialized with the power and electrical variables, heat dissipation fluxes, and time values obtained from Table 5 and Table 6 and material properties parameters of Table 4.

A preliminary frequency-transient study was conducted for one hour to establish an accurate initial temperature distribution and model transient temperature evolution. This simulation aimed to capture the heating and solid-liquid transition during the melting trial, considering the progressive temperature increment. The simulation achieved a quasi-stationary temperature state, serving as the starting point for subsequent transient dynamic melting simulations.

During the experimental trial at 1500 °C, it was found that the average applied power was 8.3 kW, and the heat transfer coefficient (HTC) of the inner coil boundary was adjusted to dissipate 5.5 kW of heat flux. However, the simulation results showed a higher melt temperature, 50 ºC, than the pyrometer reading. The observed difference falls within acceptable margins considering additional variables in experimental tests, such as dross particles on the metal, fumes, and gases, which can affect the measurement.

A sensitivity and parameterization study addressed the difference between the initially considered emissivity value for radiation and the one that best fits the target temperature of 1500 °C. The optimal emissivity value for achieving the target temperature of 1510 °C was found to be 0.35, higher than the initial value considered. The preliminary quasi-stationary frequency-transient coupled simulation results are presented in Fig. 13.

Heat flux vectors show intense heat transfer from the melt to the crucible, especially at the liquid metal-crucible contact area. The temperature distribution shows a maximum melt temperature of 1500 ºC and around 1300 °C for the thermocouples. The

subassembly of the crucible and melt box exhibits high thermal insulation capacity, rapidly reducing the temperature, while the metal maintains a relatively homogeneous temperature, to be further analyzed in the subsequent section.

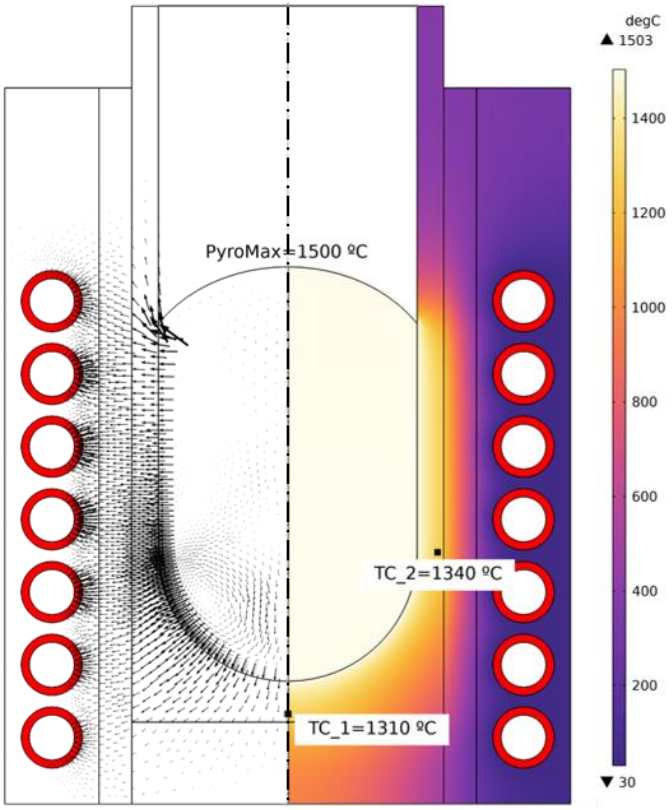

Fig. 13. Conductive heat flux vectors and temperature distribution for 8.3 kW power.

4.2.3. Transient temperature correlation

Returning to the analysis of VIM melting, the power-temperature-time data (Fig. 5) of the experimental test were employed as input parameters to simulate the temperature variations and validate the simulation results. The objective was to reproduce the two quasi-stationary temperature stages at 1500 ºC and 1450 ºC feeding the model with the electrical and heat dissipation variables resumed in the Table 5 and Table 6. The transient simulation will assess the model's response to dynamic power variations and the temperature response.

To accurately capture the temperature variations, two reference probes were placed at the exact locations of the thermocouples, while the pyrometer measured the maximum temperature of the upper melt contour. For each stage, the averaged power was used as the input, and the heat dissipation for the water-cooled coil was adjusted, as shown in Fig. 14.

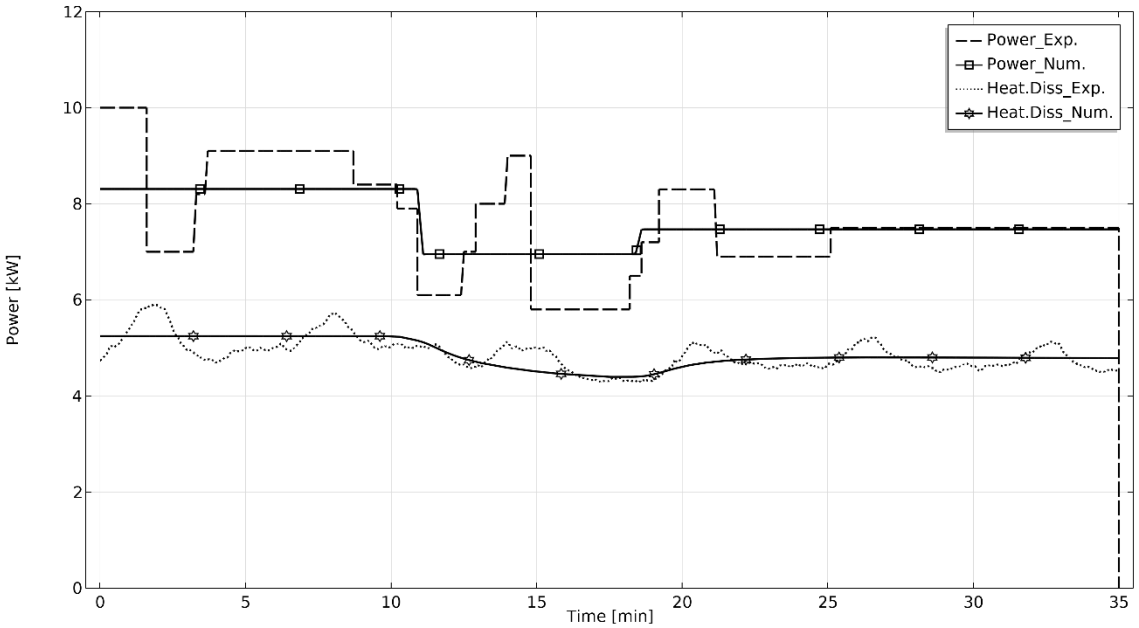

Fig. 14. Correlation between input variables applied power and dissipated heat.

The transient temperature evolution is depicted in Fig. 15, overlaid with the experimental measurements. The model reproduced temperature values with a maximum discrepancy of 20 °C for any measurement point. Although the model data did not exhibit signal interference in the experimental data, the overall trends display similar behavior during the first quasi-stationary period. The transient analysis reveals that the metallic charge had lower thermal inertia than the ceramic crucible. Once the transient stage ends, the system reaches a new steady state at 1450 °C for the metallic charge, while the ceramic crucible decreases in temperature correspondingly to around 1300 °C. In this new steady state, the model exhibited less accuracy in relative temperature terms for the thermocouple placed on the wall (TC_2).

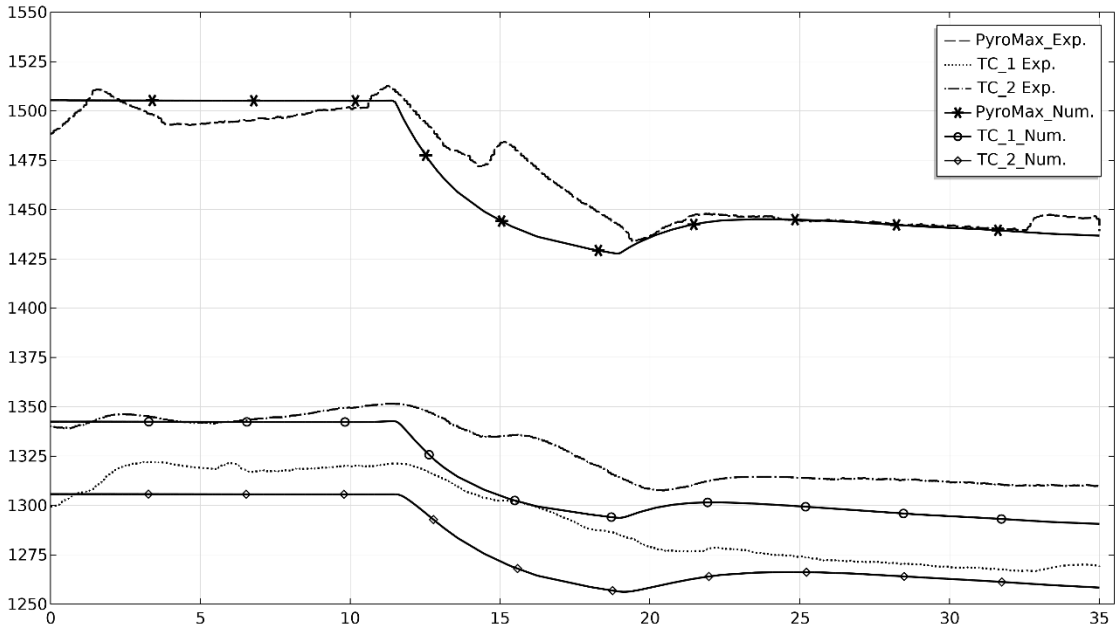

Fig. 15. Comparison of computed temperature and experimental measurement.

The dynamic temperature response of the simulation is accurate, with a relative error of 5 %, considering the temperature transition and stabilization at the two target

temperatures. The absolute temperature deviation for thermocouple TC_2 at the stationary 1450 °C is 25 °C. The melt temperature mainly influences the behavior of TC_2, as it reproduces the same trends as the metal temperature, being more sensitive to its variation.

In this regard, as was mentioned before, the thermal conductivity of the crucible plays a critical role. A sensitivity analysis was done by varying the magnitude by 10 % inside the experimental measurement uncertainty for the alumina (Al_2O_3) crucible thermal characterization. The consistency of the model was notable as it led to maximum temperature variations of 30 ºC for the pyrometer temperature reference, while for the crucible probes, there was a slight deviation.

Although the correlation could be slightly adjusted, this would result in a loss of accuracy for TC_1, which exhibits a decreasing trend. It should be noted that the simulation does not consider the power increment during the adaptation stage, where a sudden temperature change occurs, which could improve the temperature correlation.

Regarding the temperature distribution in the melt (Fig. 16), a homogeneous field is obtained with a difference of 5 °C for the two quasi-stationary stages. The homogeneous temperature distribution may be attributed to the turbulent heat transfer λ_T. Also, the low charge mass of 2 kg and low metal viscosity of 10^{-3} Pa·s produces an intense recirculation between the vortices, leading to temperature homogenization. Additionally, the thermally insulating crucible aids in maintaining metal temperature stability.

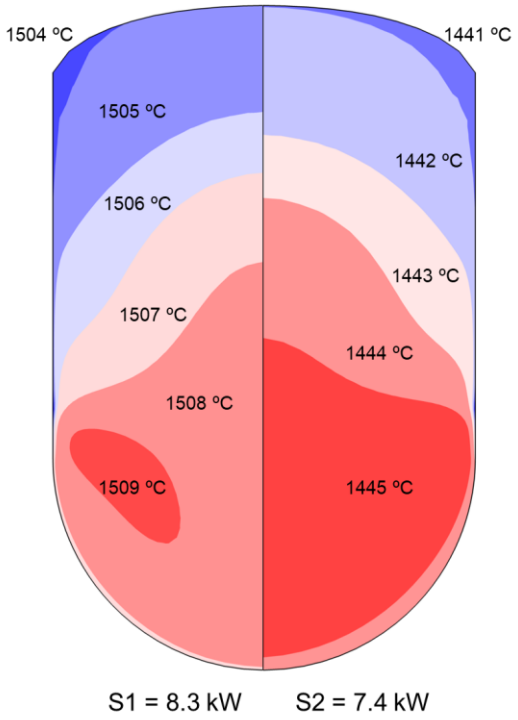

Fig. 16. Temperature contour distribution for 1ºC intervals in the quasi-stationary stages at 8.3 kW and 7.4 kW.

At the beginning of the transient study, the unknown temperature distribution of the whole system is a limiting factor. The pyrometer temperature defined the quasi-stationary condition as a local stationary condition, which does not mean a fixed condition in the rest of the domains. Furthermore, additional uncertainty artifacts, such as the accuracy of the thermocouples and pyrometer, must be considered.

In addition, it must be emphasized that the modeled power was the average value of the stages and did not account for the continuous power adjustments to maintain the objective temperatures, possibly increasing the discrepancies. On the other hand, the model does not account for the necessary time required by the power generator to couple with the resonance frequency of the equivalent circuit and the input power command. Therefore, in this time gap, the power generator might be supplying extra power, leading to a slower temperature decrease.

5. Conclusions

A coupled multiphysics numerical model was developed to simulate the nickel-based superalloy Inconel 718 temperature dynamics during the VIM process. The complex phenomena occurring during melting were simulated in a coupled formulation in a single and compact modeling structure. The modeling approach was optimized, minimizing the computation time by separating the free surface deformation and heat transfer processes.

- The ALE algorithm, employing the moving mesh method, proved effective in reproducing the free surface deformation during the VIM process. An acceptable correlation was achieved for different mass-filling levels under the 25 kW induced power conditions. The convergence and robustness of the computational model were obtained with the re-meshing process over the study steps.

- The transient temperature simulation showed a high level of accuracy, with a relative discrepancy lower than 5% for the melt temperature compared to the experimental data in both quasi-stationary and dynamic situations across all three temperature experimental references. However, the model temperature responded faster than the experimental. As the rest of the system is highly variable, minimizing the error in absolute terms is not feasible without further experimental tests to acquire more knowledge about the temperature distribution in the crucible.

- Crucible thermal conductivity plays a critical role in the heat transfer phenomena, maintaining the internal energy in the melt due to its thermal insulation properties. The temperature variation observed in the melt was approximately 5 °C, which is attributed to the continuous recirculation of the melt and high thermal conductivity due to turbulent heat transfer, which results in efficient temperature homogenization.

This experimentally validated model highlights a potential tool to determine the best VIM operating conditions facilitating the determination of an optimized melting procedure, reducing process cycle time, and enhancing energy savings at the same time avoiding the overheating of the melt.

Funding

The authors would like to sincerely thank the Basque Government and the Department of Education, Universities, and Research for its financial support by means of the Hazitek FAKTORIA project (ZE-2020/00001) program of the RVCTI.

Declaration of Competing Interest

The authors declare that they have no known competing financial interests or personal relationships that could have appeared to influence the work reported in this paper.

References

[1] T. M. Pollock and S. Tin, “Nickel-based superalloys for advanced turbine engines: Chemistry, microstructure, and properties,” *J. Propuls. Power*, vol. 22, no. 2, pp. 361–374, May 2006.

[2] E. A. Loria, “The Status and Prospects of Alloy 718,” *JOM*, vol. 40, no. 7, pp. 36–41, Jul. 1988.

[3] A. Mitchell, “Melting and Refining of Superalloys and Titanium Alloys.,” *ISIJ Int.*, vol. 32, no. 5, pp. 557–562, May 1992.

[4] A. Umbrashko, E. Baake, B. Nacke, and A. Jakovics, “Modeling of the turbulent flow in induction furnaces,” *Metall. Mater. Trans. B Process Metall. Mater. Process. Sci.*, vol. 37, no. 5, pp. 831–838, Oct. 2006.

[5] E. Baake, A. Mühlbauer, A. Jakowitsch, and W. Andree, “Extension of the k-ε model for the numerical simulation of the melt flow in induction crucible furnaces,” *Metall. Mater. Trans. B*, vol. 26, no. 3, pp. 529–536, May 1995.

[6] K. Pericleous and V. Bojarevics, “Pseudo-spectral solutions for fluid flow and heat transfer in electro-metallurgical applications,” *Prog. Comput. Fluid Dyn.*, vol. 7, pp. 118–127, 2007.

[7] F. Felten, Y. Fautrelle, Y. Du Terrail, and O. Metais, “Numerical modelling of electromagnetically-driven turbulent flows using LES methods,” *Appl. Math. Model.*, vol. 28, no. 1, pp. 15–27, Jan. 2004.

[8] P. Buliński *et al.*, “Numerical examination of the evaporation process within a vacuum induction furnace with a comparison to experimental results,” *Appl. Therm. Eng.*, vol. 150, pp. 348–358, Mar. 2019.

[9] M. Ščepanskis, A. Jakovičs, E. Baake, and B. Nacke, “Solid inclusions in an electromagnetically induced recirculated turbulent flow: Simulation and experiment,” *Int. J. Multiph. Flow*, vol. 64, pp. 19–27, Sep. 2014.

[10] C. Courtessole and J. Etay, “Flows and mass transfers in two superimposed liquid layers in an induction furnace,” *Int. J. Heat Mass Transf.*, vol. 65, pp. 893–906, Oct. 2013.

[11] S. Spitans, A. Jakovics, E. Baake, and B. Nacke, “Numerical modeling of free surface dynamics of melt in an alternate electromagnetic field: Part I. Implementation and verification of model,” *Metall. Mater. Trans. B Process Metall. Mater. Process. Sci.*, vol. 44, no. 3, pp. 593–605, 2013.

[12] C. Zhang *et al.*, “Break the superheat temperature limitation of induction skull melting technology,” *Appl. Therm. Eng.*, vol. 220, p. 119780, Feb. 2023.

[13] H. Lv, L. Kang, K. Wang, and Y. Liu, “Parametric optimization of removing iron

from solid waste melts based on analysis of real-time coupled two-phase interface in an induction heating furnace," *Energy*, vol. 261, p. 125195, Dec. 2022.

[14] A. Bansal, P. Chapelle, Y. Delannoy, E. Waz, P. Le Brun, and J. P. Bellot, "Experimental and Numerical Analysis of the Deformation of a Liquid Aluminum Free Surface Covered by an Oxide Layer During Induction Melting," *Metall. Mater. Trans. B Process Metall. Mater. Process. Sci.*, vol. 46, no. 5, pp. 2096–2109, Oct. 2015.

[15] J. Baiges, R. Codina, A. Pont, and E. Castillo, "An adaptive Fixed-Mesh ALE method for free surface flows," *Comput. Methods Appl. Mech. Eng.*, vol. 313, pp. 159–188, Jan. 2017.

[16] J. D. Lavers, "State of the art of numerical modeling for induction processes," *COMPEL - Int. J. Comput. Math. Electr. Electron. Eng.*, vol. 27, no. 2, pp. 335–349, 2008.

[17] W. Elsaady, C. Moughton, A. Nasser, and H. Iacovides, "Coupled numerical modelling and experimental analysis of domestic induction heating systems," *Appl. Therm. Eng.*, vol. 227, p. 120170, Jun. 2023.

[18] Y. Yang, R. Chen, J. Guo, H. Ding, and Y. Su, "Numerical analysis for electromagnetic field influence on heat transfer behaviors in cold crucible used for directional solidification," *Int. J. Heat Mass Transf.*, vol. 122, pp. 1128–1137, Jul. 2018.

[19] Y. Hadad, E. Kochavi, and A. Levy, "Inductive heating with a stepped diameter crucible," *Appl. Therm. Eng.*, vol. 102, pp. 149–157, Jun. 2016.

[20] M. Fisk, M. Ristinmaa, A. Hultkrantz, and L. E. Lindgren, "Coupled electromagnetic-thermal solution strategy for induction heating of ferromagnetic materials," *Appl. Math. Model.*, vol. 111, pp. 818–835, Nov. 2022.

[21] M. C. Song and Y. H. Moon, "Coupled electromagnetic and thermal analysis of induction heating for the forging of marine crankshafts," *Appl. Therm. Eng.*, vol. 98, pp. 98–109, Apr. 2016.

[22] M. H. Tavakoli, H. Karbaschi, and F. Samavat, "Influence of workpiece height on the induction heating process," *Math. Comput. Model.*, vol. 54, no. 1–2, pp. 50–58, Jul. 2011.

[23] M. Patil, R. Kumar Choubey, and P. Kumar Jain, "Influence of coil shapes on temperature distribution in induction heating process," *Mater. Today Proc.*, Sep. 2022.

[24] X. Fu, B. Wang, X. Tang, H. Ji, and X. Zhu, "Study on induction heating of workpiece before gear rolling process with different coil structures," *Appl. Therm. Eng.*, vol. 114, pp. 1–9, Mar. 2017.

[25] Y. Xiao, Y. Han, D. fu Zhao, L. min Wang, and D. Xu, "Temperature gradient control of frequency conversion heating for a thick-walled pipe based on energy transfer," *Int. J. Heat Mass Transf.*, vol. 201, p. 123589, Feb. 2023.

[26] Y. Q. Zhao, Y. Han, and Y. Xiao, "An asynchronous dual-frequency induction heating process for bevel gears," *Appl. Therm. Eng.*, vol. 169, p. 114981, Mar. 2020.

[27] L. Lu, S. Zhang, J. Xu, H. He, and X. Zhao, "Numerical study of titanium melting by high frequency inductive heating," *Int. J. Heat Mass Transf.*, vol. 108, pp. 2021–2028, May 2017.

[28] M. Fisk, “Validation of induction heating model for alloy 718 components,” *Int. J. Comput. Methods Eng. Sci. Mech.*, vol. 12, no. 4, pp. 161–167, Jul. 2011.

[29] M. Kranjc, A. Zupanic, D. Miklavcic, and T. Jarm, “Numerical analysis and thermographic investigation of induction heating,” *Int. J. Heat Mass Transf.*, vol. 53, no. 17–18, pp. 3585–3591, Aug. 2010.

[30] P. Buliński *et al.*, “Numerical and experimental investigation of heat transfer process in electromagnetically driven flow within a vacuum induction furnace,” *Appl. Therm. Eng.*, vol. 124, pp. 1003–1013, Sep. 2017.

[31] V. Bojarevics, K. Pericleous, R. A. Harding, and M. Wickins, “The development and experimental validation of a numerical model of an induction skull melting furnace,” *Metall. Mater. Trans. B*, vol. 35, no. 4, pp. 785–803, Aug. 2004.

[32] E. Baake, B. Nacke, F. Bernier, M. Vogt, A. Mühlbauer, and M. Blum, “Experimental and numerical investigations of the temperature field and melt flow in the induction furnace with cold crucible,” *COMPEL - Int. J. Comput. Math. Electr. Electron. Eng.*, vol. 22, no. 1, pp. 88–97, 2003.

[33] R. Chen *et al.*, “Glass melting inside electromagnetic cold crucible using induction skull melting technology,” *Appl. Therm. Eng.*, vol. 121, pp. 146–152, Jul. 2017.

[34] P. Garcia-Michelena *et al.*, “Effect of the crucible composition on the Inconel 718 vacuum induction melting process efficiency,” *J. Mater. Res. Technol.*, Feb. 2023.

[35] J. D. Jackson, *Classical Electrodynamics*, 3rd ed. John Wiley & Sons, 1999.

[36] D. C. Wilcox, *Turbulence Modeling for CFD*, 2nd ed. DCW Industries, 1998.

[37] R. Scardovelli and S. Zaleski, “Direct numerical simulation of free-surface and interfacial flow,” *Annu. Rev. Fluid Mech.*, vol. 31, no. 1, pp. 567–603, 1999.

[38] D. Kuzmin, O. Mierka, and S. Turek, “On the implementation of the fr-fturbulence model in incompressible flow solvers based on a finite element discretisation,” *Int. J. Comput. Sci. Math.*, vol. 1, no. 2–4, pp. 193–206, 2007.

[39] R. B. Bird, W. E. Stewart, and E. N. Lightfoot, *Transport Phenomena.* John Wiley & Sons, 2007.

[40] B. Weigand, J. R. Ferguson, and M. E. Crawford, “An extended Kays and Crawford turbulent Prandtl number model,” *Int. J. Heat Mass Transf.*, vol. 40, no. 17, pp. 4191–4196, Oct. 1997.

[41] K. Abe, T. Kondoh, and Y. Nagano, “A new turbulence model for predicting fluid flow and heat transfer in separating and reattaching flows—I. Flow field calculations,” *Int. J. Heat Mass Transf.*, vol. 37, no. 1, pp. 139–151, Jan. 1994.

[42] K. C. Mills, *Recommended values of thermophysical properties for selected commercial alloys*. Woodhead Publishing, 2002.

[43] X. Chamorro, N. Herrero-Dorca, D. Bernal, and I. Hurtado, “Induction Skull Melting of Ti-6Al-4V: Process Control and Efficiency Optimization,” *Metals (Basel).*, vol. 9, no. 5, p. 539, May 2019.

[44] M. Leitner, T. Leitner, A. Schmon, K. Aziz, and G. Pottlacher, “Thermophysical Properties of Liquid Aluminum,” *Metall. Mater. Trans. A Phys. Metall. Mater. Sci.*, vol. 48, no. 6, pp. 3036–3045, Jun. 2017.